energies

MDPI

Article

Morphology Regulated Hierarchical Rods-, Buds-, and Sheets-like $CoMoO_4$ for Electrocatalytic Oxygen Evolution Reaction

Kumcham Prasad [1], Neelima Mahato [1], Kisoo Yoo [2,*] and Jonghoon Kim [1,*]

[1] Energy Storage and Conversion Laboratory, Department of Electrical Engineering, Chungnam National University, Daejeon 34134, Republic of Korea
[2] School of Mechanical Engineering, Yeungnam University, Gyeongsan-si 38541, Republic of Korea
* Correspondence: kisooyoo@yu.ac.kr (K.Y.); whdgns0422@cnu.ac.kr (J.K.)

Abstract: One of the hugely focused areas of research for addressing the world's energy and environmental challenges is electrochemical water oxidation. Morphological modulation of nanomaterials is essential for producing efficient electrocatalysts to achieve the required results. The purpose can be achieved by controlling synthesis parameters, and this is a key factor which greatly influences the oxygen evolution reaction (OER) performance during electrochemical water splitting. In this study, synthesis of cobalt molybdate ($CoMoO_4$) through a simple and low-cost hydrothermal/solvothermal strategy with tunable morphology is demonstrated. Different morphologies, namely rods-like, buds-like, and sheets-like, referred to as R-CMO, B-CMO, and S-CMO, respectively, have been obtained by systematically varying the solvent media. Their catalytic activity towards OER was investigated in 1.0 M aqueous KOH medium. R-CMO nanoparticles synthesized in an aqueous medium demonstrated the lowest overpotential value of 349 mV to achieve a current density of 10 mA cm^{-2} compared with other as-prepared catalysts. In contrast, the B-CMO and S-CMO exhibited overpotential values of 369 mV and 384 mV, respectively. Furthermore, R-CMO demonstrated an exceptional electrochemical stability for up to 12 h.

Keywords: $CoMoO_4$ nanoparticles; morphology evolution; electrocatalyst; oxygen evolution reaction

check for updates

Citation: Prasad, K.; Mahato, N.; Yoo, K.; Kim, J. Morphology Regulated Hierarchical Rods-, Buds-, and Sheets-like $CoMoO_4$ for Electrocatalytic Oxygen Evolution Reaction. *Energies* **2023**, *16*, 2441. https://doi.org/10.3390/en16052441

Academic Editor: Adriano Sacco

Received: 27 January 2023
Revised: 19 February 2023
Accepted: 1 March 2023
Published: 3 March 2023

1. Introduction

Clean, renewable, and environmentally friendly energy systems that use conversion and storage technologies include water splitting, fuel cells, metal–air/oxygen batteries, and carbon dioxide/nitrogen fixation. These systems offer promising solutions for the current energy crisis and environmental issues. For instance, electrochemical methods in conjunction with energy conversion technologies can be used to produce sustainable chemicals and fuels such as H_2, CH_4, NH_3, and HCOOH. Prominently, the Earth's atmosphere supplies the feedstock of water, air/oxygen, carbon dioxide, and nitrogen. However, a large overpotential that is above thermodynamic criteria still hinders the development of these promising technologies. As a result, developing high-performance electrocatalysts is critical. The oxygen evolution reaction (OER), oxygen reduction reaction (ORR), hydrogen evolution reaction (HER), nitrogen reduction reaction (N2RR), and carbon dioxide reduction reaction are the main reactions in heterogeneous electrocatalysis [1–3].

Electrochemical water splitting with high purity hydrogen production without CO_2 emissions is one of the best methods for establishing a sustainable energy landscape. Because of the abundant supply of raw materials such as power and water, electrochemical water splitting outperforms coal gasification and steam–methane reformation in terms of high hydrogen generation. Particularly, the alkaline water electrolysis has drawn a lot of attention due to its attributes of simple construction and inexpensive electrode materials. The viability of these technologies depends on the electrochemical performance of the two half-reactions, namely the oxygen evolution reaction and the hydrogen evolution reaction taking place at the anode and cathode, respectively. Furthermore, the OER is an electron–proton coupled, complicated, stepwise reaction that is thermodynamically uphill. As a result, compared to the HER process, the OER is a bottleneck in the entire process and requires a high overpotential to achieve the appropriate current density.

As a result, more efforts have been put into creating high-performance and affordable electrocatalysts, particularly OER catalysts. The standard electrocatalysts for OER and HER are frequently recognized as Ir/Ru and Pt-based materials, respectively. Unfortunately, because of their high cost, limited availability, and poor stability under harsh reaction circumstances, these materials are not extensively usable in the context of sustainable energy use technologies. As a result, materials based on transition metals that are Earth-abundant have generated a lot of attention as OER and HER electrocatalysts. Metals/alloys, metal oxides, (oxy)hydroxides, single-atom catalysts, and carbon-based compounds are a few examples of these substances [4–6]. In this regard, exploring highly active, affordable, and Earth-abundant OER electrocatalysts is extremely desirable. Some of the recently used OER electrocatalysts to replace the precious catalysts are metal oxides/hydroxides [7–9], metal sulfides [10,11], metal selenides [12,13], metal nitrides [14,15], and metal phosphides [16–18]. In this context, transition-metal molybdates have drawn huge interest among researchers due to their strong electrocatalytic activity, low cost, and environmental compatibility [19].

Due to synergistic association between the high redox behavior of Cobalt (Co) and the strong electrical conductivity of Molybdenum (Mo), $CoMoO_4$ behaves as a remarkable OER electrocatalyst [20–22]. However, because of the small number of active sites, it exhibits relatively poor charge transport efficiency and structural coarsening. During long cycles, the OER activity of $CoMoO_4$ is still not sufficient [23]. In this regard, an efficient plan to increase the OER activity of $CoMoO_4$ catalysts is highly anticipated. Morphology tuning is one of the effective methods for addressing the issue by increasing the specific surface area to enhance the number of active sites. For example, B. Paul et al. synthesized morphology controlled Co_3O_4 nanoparticles using facile hydrothermal strategy by varying the reaction time over 6, 12 and 24 h. The Co_3O_4-24 h catalyst is reported to show an overpotential of 296 mV to achieve a current density of 10 mA cm^{-2} [24]. X. Lv et al. synthesized a morphology controlled Cu_2S/CF composite by varying the ratio of solvents in a hydrothermal reaction containing alcohol and water in a ratio of 1:9 and exhibited an overpotential of 239 mV to achieve a current density of 10 mA cm^{-2} [25].

W. Xie et al. synthesized Fluorine doped $CoMoO_4$ on graphene felt to achieve an enhanced number of active sites and delivered an overpotential of 256 mV at the current density of 10 mA cm^{-2} [26]. Using a simple hydrothermal process, M.Q. Yu et al. synthesized $CoMoO_4$ that resembled porous flowers to show an overpotential of 312 mV at a current density of 10 mA cm^{-2} [20]. Y. Xu et al. also used a simple hydrothermal process to construct $Ni(OH)_2$ nanosheets wrapped around $CoMoO_4$ nanoplate arrays supported on Ni foam to reveal an overpotential of 349 mV at a current density of 100 mA cm^{-2} [27]. A hybrid of cobalt oxide nanoparticles anchored on $CoMoO_4$ nanorods synthesized by S. Xun et al. exhibited good oxygen evolution catalytic activity with a low overpotential of 253 mV at a current density of 10 mA cm^{-2} [19]. The hierarchical $CoMoO_4$ nanoparticle-decorated nanoplate arrays that X. Guan et al. grew on Ni foam showed an overpotential of 317 mV to achieve a current density of 100 mA cm^{-2} [28]. Hollow nanocages of Co_3O_4-$CoMoO_4$ heterostructures synthesized by J. Luo et al. showed an overpotential of 248 mV to afford a current density of 10 mA cm^{-2} [29]. $CoMoO_4$ nanofilms on $ZnCo_2O_4$ nanosheets grown on Ni foam were synthesized by W.D. Yang et al. using a simple two-step hydrothermal technique and showed a low overpotential of 237 mV at 20 mA cm^{-2} [30]. Using a simple hydrothermal process, L. Xia et al. synthesized hollow porous Co_3O_4/$CoMoO_4$ and showed good oxygen evolution reaction performance with an overpotential of 342 mV at 100 mA cm^{-2} [31].

Despite the fact that many studies using various $CoMoO_4$ morphologies and composites for the oxygen evolution reaction have been published, there are still numerous ways to modify the morphology of the catalysts to improve their performance. In this work, a novel strategy to synthesize morphology controlled $CoMoO_4$ nanoparticles is proposed. Different nanoparticles of $CoMoO_4$ with rods-like, buds-like, and sheets-like morphologies were synthesized using a facile hydrothermal/solvothermal method utilizing water, water/ethanol and water/ethyleneglycol (in 1:1, *v*/*v*) as solvent media, respectively. The material's physicochemical properties were studied using different analytical techniques. The electrocatalytic activity of the prepared electrodes with regard to oxygen evolution reaction was systematically studied. The R-CMO electrode outperformed the other two electrodes with an overpotential of 349 mV to achieve a current density of 10 mA cm^{-2}, whereas the B-CMO and S-CMO exhibited an overpotential of 369 and 384 mV, respectively. Thus, the R-CMO electrode is anticipated to be a viable electrode material with appreciable electrocatalytic activity for oxygen evolution reaction.

2. Experimental

2.1. Materials

Analytical grade chemicals were employed in the experiment exactly as they were received. Sigma Aldrich Co., South Korea provided the $Co(NO_3)_2{\cdot}6H_2O$ (cobalt nitrate hexahydrate), and $Na_2MoO_4{\cdot}2H_2O$ (sodium molybdate dihydrate). Daesung Chemicals in South Korea supplied the ethanol and ethyleneglycol.

2.2. Synthesis of $CoMoO_4$ Nanostructured Materials

Different nanostructured particles of $CoMoO_4$ were synthesized via simple hydrothermal and solvothermal methods with subsequent annealing treatment. In a typical synthesis procedure, 50 mmol of cobalt nitrate hexahydrate and 50 mmol of sodium molybdate dihydrate were dissolved in 150 mL of DI water, and continuously stirred until a homogeneous mixture was formed. The solution was then transferred to a 200 mL Teflon tube and placed in stainless steel autoclave unit and heated to a temperature of 180 °C for 12 h. Post synthesis, the autoclave unit was allowed to cool down to ambient temperature. The resultant precipitate formed in the autoclave unit was thoroughly washed with water and ethanol to remove undesired particles. Then, the powders were dried at a temperature of 80 °C overnight followed by annealing at an elevated temperature of 400 °C in air for 4 h to obtain rods-like $CoMoO_4$. For synthesizing buds-like $CoMoO_4$ and sheets-like $CoMoO_4$, mixtures of water and ethanol (1:1, *v*/*v*), and water and ethyleneglycol (1:1, *v*/*v*) were used as solvents, respectively, keeping all the remaining reaction parameters unchanged. The detailed synthesis procedure is illustrated in Scheme 1.

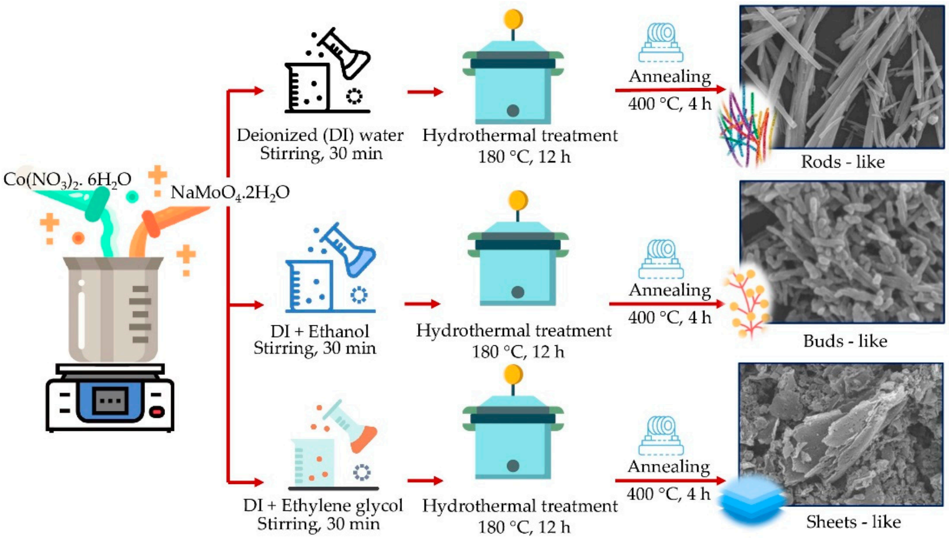

Scheme 1. Schematic illustration of synthesis procedure for the rods-, buds-, and sheets-like $CoMoO_4$ electrocatalysts.

2.3. Materials Characterization

X-ray diffractometry (XRD, PANalytical X'Pert Pro with Cu K radiation source of wavelength = 1.540 A°) was used to analyze the crystal structures and phase purity of the prepared samples. Fourier transform infrared spectroscopy (FT-IR, Perkin Elmer, Waltham, MA, USA) was used to analyze the chemical bonds present in the materials. A field-emission scanning electron microscopy (FESEM, S-4800, Hitachi, Japan) with an X-ray column attached was used to examine the samples' surface morphology and elemental composition. High-resolution transmission electron microscopy was performed using (HRTEM, Tecnai G^2 F20 S-Twin, Hillsboro, OR, USA) with a field-emission electron gun in Schottky mode set to 200 kV. The composition and oxidation states of the materials were examined using X-ray photoelectron spectroscopy (XPS, K-alpha, Thermo Scientific, Waltham, MA, USA) with Al K X-ray as monochromatic radiation source (1486.6 eV).

2.4. Electrochemical Characterization

In a 1.0 M KOH aqueous electrolyte that had been nitrogen-purged, all electrochemical experiments were conducted using a Biologic VSP-150 electrochemical workstation in a three-electrode cell, using the Hg/HgO as reference electrode, Platinum (Pt) mesh as counter electrode, and as-prepared $CoMoO_4$ material as working electrode. The working electrode was prepared using a slurry comprising active material, conductive carbon block, and poly(vinylidene fluoride) with a weight percentage of 80:10:10. Then, the obtained slurry was coated onto a pretreated Ni foam (1 × 1 cm^2) and dried at 80 °C overnight. The mass of the active material present on the electrodes was determined by weighing before and after coating and determined to be ~2 mg cm^{-2}.

The following Nernst equation was used to modify all of the potentials in this work in relation to the reversible hydrogen electrode (*RHE*) [32]:

$$E_{RHE} = 0.095 + E_{Hg/HgO} + 0.0591\ p^{H} \tag{1}$$

The polarization curves were measured at 5 mV s^{-1} and the double-layer capacitance (C_{dl}) values were determined using cyclic voltammetry (CV) measurements in the non-faradaic potential region between 1.15 and 1.25 V vs. *RHE* at various scan rates of 10, 20, 30, 40, 50, 60, and 70 mV s^{-1}. The value of C_{dl} in mF is obtained from the linear slope values obtained by graphing the current density differences (ΔJ) against the scan rates. Electrochemical active surface area (*ECSA*) is calculated using the Equation (2):

$$ECSA = \frac{C_{dl}}{C_s} \tag{2}$$

where the C_s value is 0.04 mF cm^{-2} in alkaline electrolyte [33], and C_{dl} is the double-layer capacitance. Electrochemical impedance spectroscopy (EIS) is measured in the frequency range of 100 MHz to 100 mHz.

3. Results and Discussion

3.1. Phase and Microstructural Analysis

An X-ray diffraction (XRD) study was used to analyze the $CoMoO_4$ material's crystalline structure and phase purity. According to the typical pattern of $CoMoO_4$ as shown in Figure 1a, all distinct diffraction peaks are accurately indexed to their respective planes of reflection. Additionally, the XRD pattern reveals that the samples are monoclinic crystals and belong to the space group $C2/m$ with space group number 12 [34]. The diffraction peak positions corresponding to the three $CoMoO_4$ samples located around the 2θ values of 13.14, 19.04, 23.24, 25.45, 26.42, 27.14, 28.37, 32.01, 33.66, 36.70, 38.75, 40.15, 43.42, 45.17, 47.48, 52.04, 53.46, 58.27, 60.04, and 64.44° are attributed to their respective planes of reflection (hkl) values of (001), (−201), (021), (201), (002), (−112), (−311), (−131), (−222), (400), (040), (003), (−422), (113), (241), (−204), (−441), (024), (−424), and (243). As there are no additional peaks except those characteristic of $CoMoO_4$ in the XRD pattern, this indicates the as-synthesized samples are phase pure.

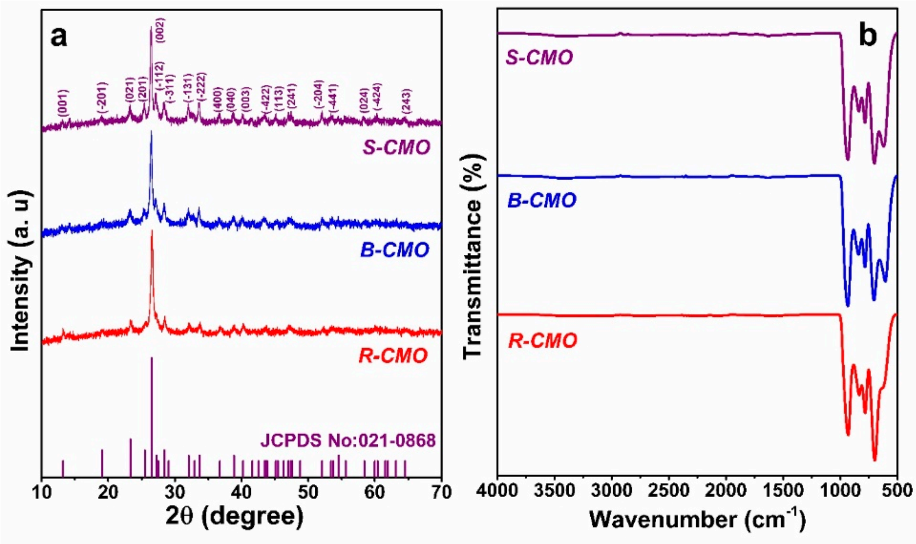

Figure 1. (**a**) XRD pattern and (**b**) FTIR spectra of synthesized $CoMoO_4$ nanostructured materials.

In addition, using the following equations (Equations (1) and (2)) the crystallite sizes (D) of the nanostructured materials are determined to be 84.62, 97.16, and 148.09 nm and the cell volumes (v) are 635.51, 637.53, and 644.01 $Å^3$, corresponding to R-CMO, B-CMO, and S-CMO, respectively [35,36].

$$\text{Crystallite size } (D) = \frac{K\lambda}{Hcos\theta} \tag{3}$$

$$\text{Cell volume } (v) = abc{\cdot}sin\beta \tag{4}$$

where D is crystallite size in nm, K is shape factor (0.9), λ is wavelength of the X-rays (0.1540598 nm for Cu $K_{\alpha 1}$ radiation), H is full width at half maximum intensity in radians, and θ is peak position in degrees. The parameters, a, b, c, and β are lattice constants.

The bonding nature in $CoMoO_4$ material was assessed using Fourier transform infrared (FT-IR) spectroscopy in the wavenumber range of 500–4000 cm^{-1} as shown in Figure 1b. The spectra of all the three samples appear almost identical, indicating that the three samples have similar compositions. Peaks appearing at 614 and 700 cm^{-1} are attributed to the vibrational mode of Mo-O and v_3 vibrational mode of MoO_4 in $CoMoO_4$. The sharp peaks appearing at 783 and 838 cm^{-1} represent the stretching vibrations of Mo-O-Mo. The stretching vibration of MoO_4 in $CoMoO_4$ is represented by the band at 932 cm^{-1}. The bands near 1600 cm^{-1} and 3400 cm^{-1} appear due to bending and stretching vibrations of the OH^- group on the material's surface [37–39].

The as-synthesized $CoMoO_4$ samples were further analyzed using SEM, to understand their morphological features and are shown in Figure 2. The utilization of different solvents apparently influenced the morphologies of the nanostructured materials. When DI water was used as a solvent medium, rods-like particles with several micrometre lengths were obtained (Figure 2a–c). Buds-like nanostructured particles were obtained when a mixture of DI water and ethanol was used as a solvent (Figure 2d–f). However, when a mixture of DI water and ethyleneglycol was used as a solvent, sheets-like nanostructured particles were obtained (Figure 2g–i). The rods-like particles appear to be aligned randomly with more void spaces in between. In contrast, the buds-like, and sheets-like particles were formed bulkily with relative fewer void spaces in between. Consequently, the effective contact area of the rods-like particles is greater compared with buds-like, and sheets-like particles. This is anticipated to enhance the utilization of more electroactive sites to interact with the electrolyte and improve the electrocatalytic performance of the electrode [40,41]. Furthermore, the EDS spectrum (Figure 2j) of the R-CMO confirms the presence of the individual elements in $CoMoO_4$.

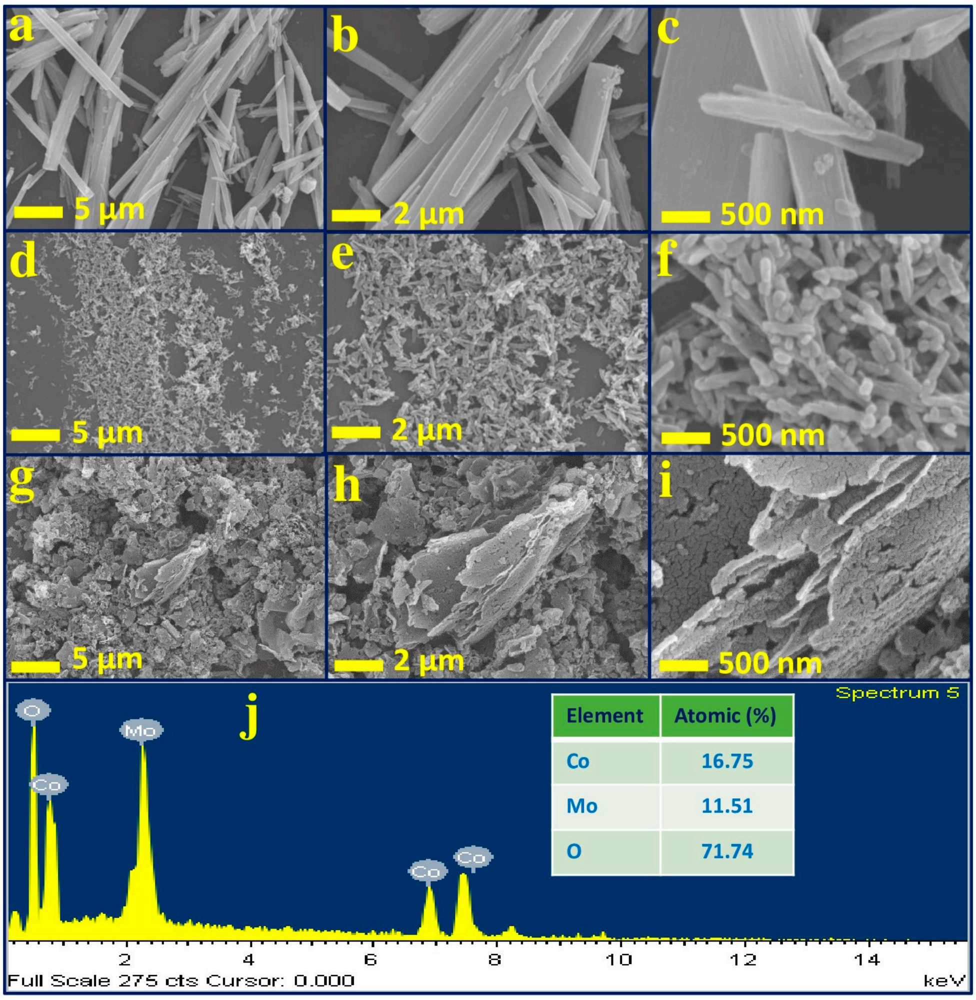

Element	Atomic (%)
Co	16.75
Mo	11.51
O	71.74

Figure 2. Low- and high-magnification SEM images of R-CMO (**a**–**c**), B-CMO (**d**–**f**), S-CMO (**g**–**i**) and EDS spectrum of R-CMO (**j**).

The TEM analysis was further used to evaluate the particle formation and self-assembly of the as-prepared $CoMoO_4$ samples. TEM analysis was performed for the R-CMO catalyst due to its superior electro-catalytic activity compared with the other two electrodes. The low- and high-resolution TEM images are shown in Figure 3a–c. The nanostructured particles, as observed in the TEM image, are primary particles for the formation of rod-like morphologies through the self-assembly process [42]. The interplanar distance was determined to be 0.39 nm corresponding to the lattice plane (021), which is also consistent with the XRD analysis. The selected area electron diffraction (SAED) pattern (Figure 3d) of the sample demonstrates its polycrystalline nature. The lattice planes of the SAED pattern are indexed according to their d-spacing values as determined using ImageJ software.

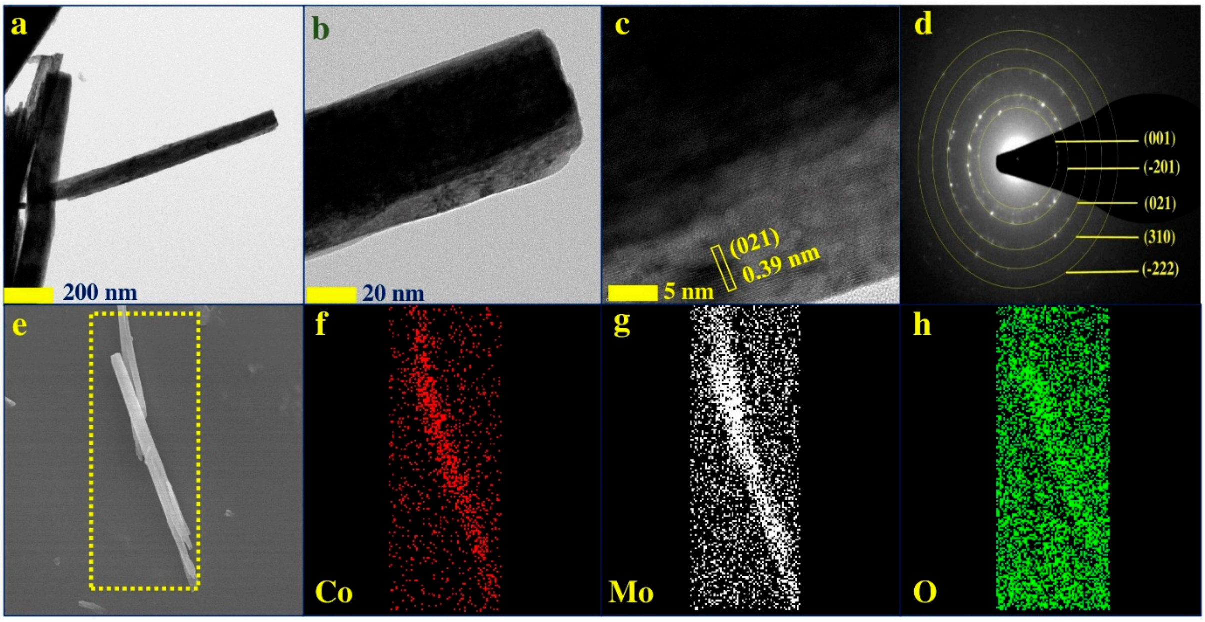

Figure 3. Low and high magnification TEM images (**a**–**c**), SAED pattern (**d**) of R-CMO and its corresponding elemental mapping (**e**–**h**).

The R-CMO sample was further investigated using X-ray photoelectron spectroscopy (XPS) to study the surface-chemical composition and chemical states attributed to its superior electrochemical performance compared with the other two specimens, as shown in Figure 4. The XPS survey scan is displayed in Figure 4a, indicating the R-CMO sample contained Co, Mo, and O species. Figure 4b depicts the Co 2*p* core level spectrum. The spin-orbit states of Co $2p_{1/2}$, Co $2p_{3/2}$, and their related satellite peaks were identified in four regions. The +3 and +2 oxidation states of the spectrum were further divided into two peaks. The peaks appearing at 780.3 eV (Co1), and 781.5 eV (Co2) belong to Co $2p_{3/2}$, and 796.1 eV (Co3), and 797.3 eV (Co4) belong to Co $2p_{1/2}$, respectively, and reflect the Co^{3+} and Co^{2+} states of Co. Similarly, Co $2p_{3/2}$ and Co $2p_{1/2}$ have satellite peaks appearing at 787.3 eV and 803.1 eV, respectively [43,44]. Additionally, the presence of the Co^{2+} oxidation state is confirmed by the energy gap of 16.2 eV between the two main peaks [43,45]. In the Mo 3*d* spectrum, two splitting doublets associated with the Mo $3d_{5/2}$ and Mo $3d_{3/2}$ states are found to appear at 231.9 and 235.1 eV, respectively, as shown in Figure 4c. It demonstrates that the molybdenum in the R-CMO sample is in the Mo^{6+} oxidation state. Additionally, it is also confirmed by the difference of ~3.6 V in binding energy between the Mo $3d_{5/2}$ and Mo $3d_{3/2}$ states [43,45]. The XPS spectra of O 1*s* was depicted in Figure 4d and is fitted into two peaks, designated as O1 and O2, located at 530.2 and 531.7 eV, respectively. The M-O bond and M-OH bond (M = Mo and Co) of the surface-adsorbed water molecules present on the surface of the material, respectively, are represented by the O1 peak and O2 peak, respectively [46,47]. Thus, the XPS study confirms the successful formation of $CoMoO_4$.

3.2. OER Performance

In a nitrogen gas-saturated solution of 1.0 M aqueous KOH, the electrocatalytic performance of the nanostructured materials towards oxygen evolution reaction was assessed using cyclic voltammetry (CV), linear seep voltammetry (LSV), and electrochemical impedance spectroscopy (EIS). The OER polarization curves of the R-CMO, B-CMO, and S-CMO catalysts with IR correction are shown in comparison with that of the bare Ni substrate in Figure 5a. The overpotential values of the catalysts are found to be 349, 369, and 384 mV corresponding to R-CMO, B-CMO, and S-CMO, with onset potentials of 1.580, 1.599, and 1.614 V vs. *RHE*, respectively, to achieve a current density of 10 mA cm^{-2}. The overpotentials of the three catalysts are observed to be nearly identical, with a small difference of about 20 mV. However, R-CMO catalyst is found to exhibit higher electrocatalytic activity compared with the other two as-prepared catalysts and evidenced by its lower overpotential and onset potential. The smaller crystallite size and higher active surface area of R-CMO are the main factors influencing its performance. These are also the main driving forces in promoting ion transportation across the void spaces and boosting the electrocatalytic OER activity [24]. The overpotential of R-CMO catalyst outperformed many previously reported non-noble metal OER electrocatalysts (Table 1).

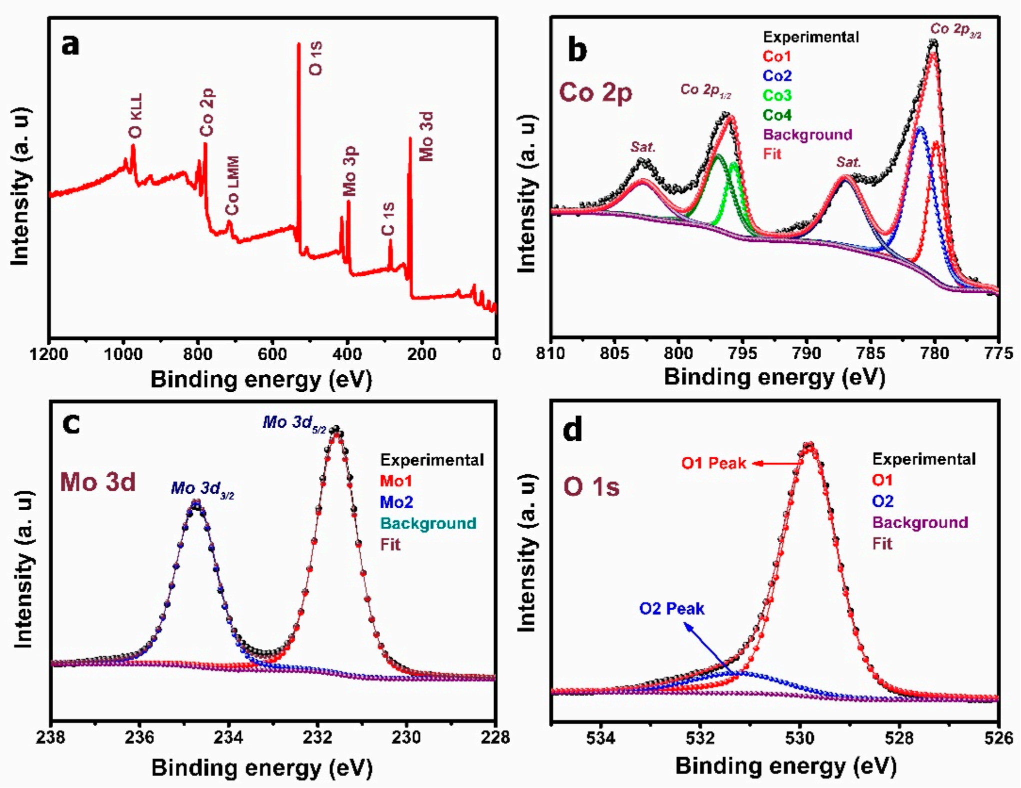

Figure 4. (**a**) XPS survey scan spectrum, core level spectra of (**b**) Co 2*p*, (**c**) Mo 3*d* and (**d**) O 1*s* for R-CMO catalyst.

The Tafel slopes of the polarization curves of the catalytic materials are determined based on LSV curves using equation, $\eta = b \log j + a$, here η represents overpotential, b stands for Tafel's slope, j for current density, and a is the constant, as shown in Figure 5b [19]. The Tafel slope of R-CMO is 165 mV decade^{-1}, which is a smaller value compared with 168 mV decade^{-1} corresponding to B-CMO and 180 mV decade^{-1} corresponding to S-CMO indicating higher catalytic kinetics towards OER process. The EIS was also used to investigate the reaction kinetics of the catalysts. The EIS measurements were conducted for all the catalysts at the potentials of their corresponding overpotentials vs. Hg/HgO obtained from the respective LSV curves, i.e., 0.63, 0.67, and 0.68 V for R-CMO, B-CMO, and S-CMO, respectively. Figure 5c depicts the Nyquist plots of the catalysts. R-CMO catalyst has a lower charge transfer resistance (R_s) of 1.30 Ω compared with B-CMO (1.37 Ω) and S-CMO (1.44 Ω) catalysts, indicating its faster kinetics towards OER activity [19].

Furthermore, as shown in Figure 5d, CV measurements were performed at various scan rates in the non-faradaic region to determine the electrochemically active surface area (*ECSA*) and double layer capacitance (C_{dl}) using Equation (2). The *ECSA* and (C_{dl}) values of R-CMO, B-CMO, S-CMO are 459, 424, and 385 cm^2, and 18.4, 16.9, and 15.4 mF cm^{-2}, respectively. The higher *ECSA* and C_{dl} values corresponding to R-CMO catalyst indicate the exposure of its large number of electroactive sites to interact with the electrolyte facilitating the OER performance [19].

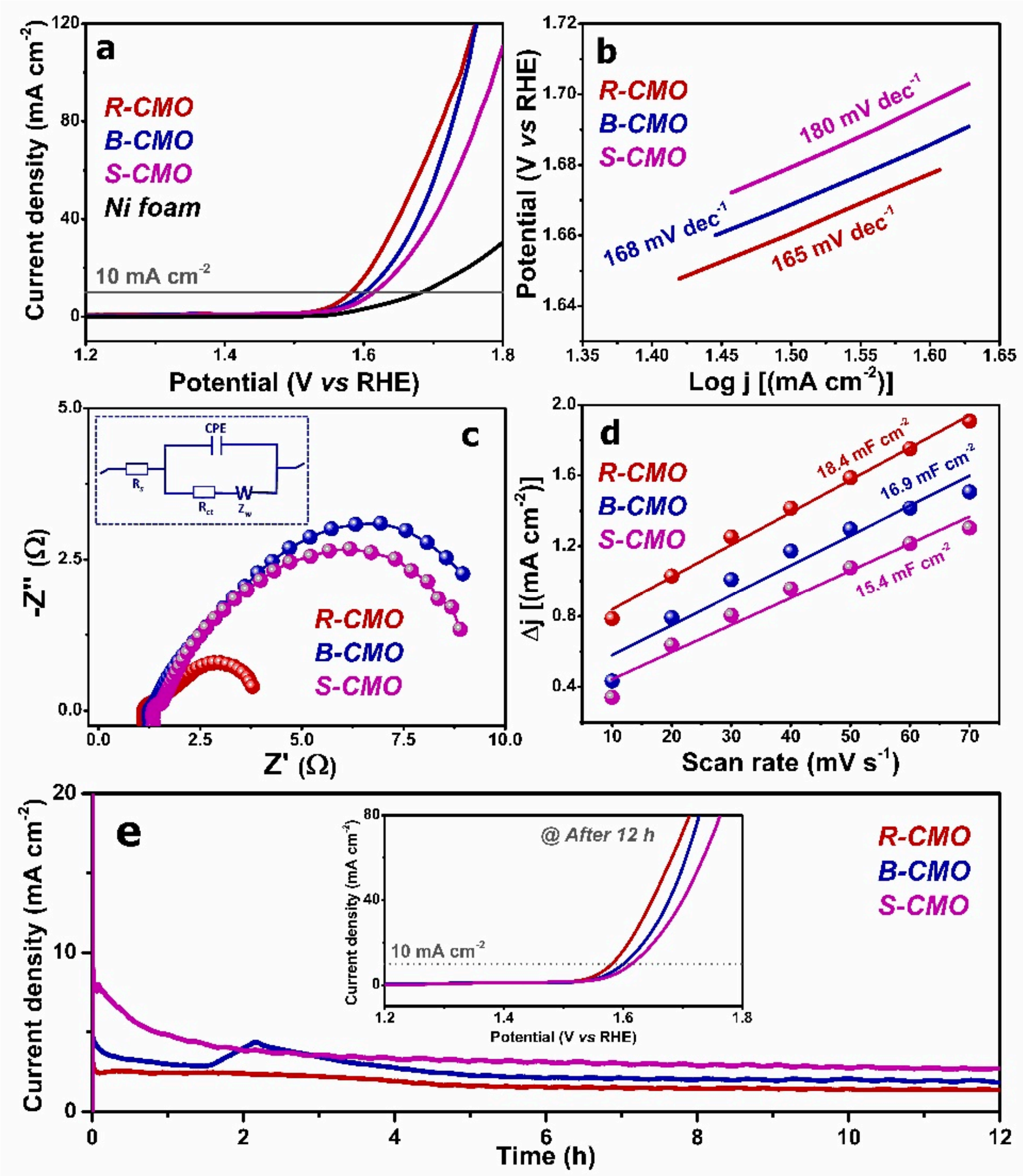

Figure 5. (**a**) Polarization curves, (**b**) Tafel curves, (**c**) EIS curves (Inset: equivalent circuit diagram), (**d**) current density differences vs. scan rates curves and (**e**) chronoamperometry stability test curves of $CoMoO_4$ nanostructured materials (Inset: Polarization curves after stability test).

Furthermore, the chronoamperometric current-time (*i-t*) stability test was conducted at the overpotentials vs. Hg/HgO of the respective catalysts to evaluate the long-term durability of the catalysts as depicted in Figure 5e. The R-CMO catalyst exhibited a relatively high stability up to 12 h with no apparent change in the current density, compared with the other two catalysts. On the other hand, in the cases of B-CMO and S-CMO catalysts, the current response was observed to be unstable in the beginning because of gradual activation of the electrode material. However, after 5 h, the current response was stable and continued to be stable for up to 12 h. The polarization curves of the three catalysts after *i-t* stability test exhibit negligible changes as depicted in the inset of Figure 5e. The *ECSA* curves of the three samples are shown in Figure 6.

Table 1. Comparison of OER performance of present work with some of the representative non-noble catalysts.

Catalyst	**Substrate**	**Electrolyte**	**Overpotential (mV) @ Current Density (mA cm^{-2})**	**References**
R-CMO	Ni foam	1.0 M KOH	349@10	This work
MWCNT/Au/Co_3O_4	GCE	1.0 M KOH	350@10	[48]
Zn-$CoSe_2$ Nanosheets	Carbon fabric collector	1.0 M KOH	356@10	[49]
Co/CeO_2	GCE	1.0 M KOH	365@10	[50]
B-CMO	Ni foam	1.0 M KOH	369@10	This work
Co_2P/NPCNTs	GCE	1.0 M KOH	370@10	[51]
Co/ZrO_2	GCE	1.0 M KOH	373@10	[50]
NiCo Nanocages	GCE	1.0 M KOH	380@10	[52]
S-CMO	Ni foam	1.0 M KOH	384@10	This work
Co/TiO_2	GCE	1.0 M KOH	390@10	[50]
$NiCo_2O_4$ Nanoflakes/Ti_4O_7	GCE	1.0 M KOH	398@10	[53]
CoP Hollow polyhedrons	GCE	1.0 M KOH	400@10	[54]
CeO_2/$Co(OH)_2$	GCE	1.0 M KOH	410@10	[55]

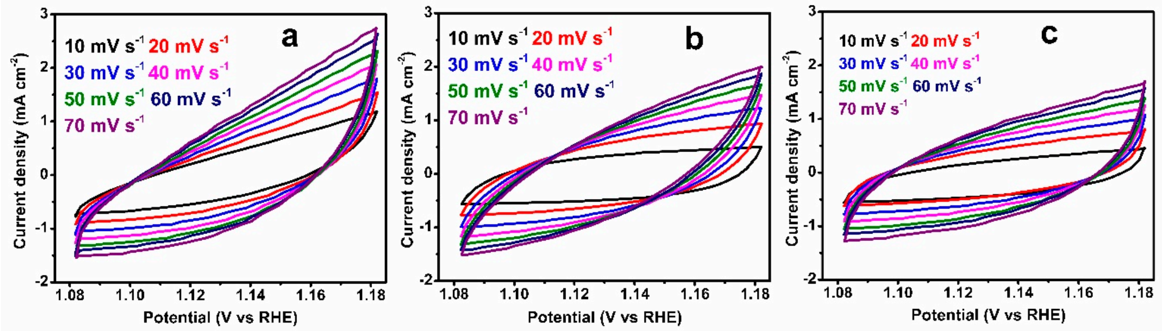

Figure 6. *ECSA* curves of (**a**) R-CMO, (**b**) B-CMO and (**c**) S-CMO catalysts.

The following features can be attributed to the higher performance of the R-CMO catalyst.

1. The R-CMO catalyst, which has a hierarchical structure made up of a number of rod-like nanostructures, utilizes the Co and Mo ions' synergistic effect to encourage adequate exposure of a number of active sites to the electrolyte solution, which enhances electrochemical stability and OER performance.
2. Rapid ion transportation is made possible by the catalyst's high electrochemically active surface area, which also offers readily accessible electroactive sites. By reducing electrode resistance, this feature also improves redox diffusion kinetics.
3. The R-CMO catalyst's void space, adorned with many nanostructured rods, increases internal stress and volumetric fluctuations to shield the active material from structural collapse and loosening of the electrical structure during the chronoamperometric stability test.

Based on the above findings, R-CMO could be used as an efficient and high-performing electrocatalyst for OER applications.

4. Conclusions

In conclusion, we described a simple hydrothermal/solvothermal approach to synthesizing $CoMoO_4$ nanostructured materials with rods-like, buds-like, and sheets-like morphologies which involves altering the solvent media during the synthesis process. The R-CMO catalyst synthesized using water as the solvent medium exhibits lower overpotential of 349 mV to afford a current density of 10 mA cm^{-2} with a Tafel's slope of 165 mV $decade^{-1}$. When compared with the performance of other catalysts, R-CMO exhibits higher OER performance, which can be attributed to its smaller crystallite size and higher active surface area. This could be the main factor promoting ion transport across void spaces and boosting electrochemical OER activity. Additionally, the chronoamperometry studies demonstrated the R-CMO catalyst's exceptional stability compared with other catalysts. Thus, the rods-like $CoMoO_4$ (R-CMO) with higher electrocatalytic OER performance has a great deal of potential for fabricating effective, inexpensive, and widely accessible alternatives for electrochemical water oxidation in place of expensive noble metal based electrocatalysts.

Author Contributions: Conceptualization, K.P. and K.Y.; Formal analysis, K.P. and N.M.; Funding acquisition, J.K. Methodology, N.M. and J.K.; Resources, J.K.; Supervision, K.Y.; Validation, N.M.; Writing—original draft, K.P.; Writing—review & editing, K.Y. and J.K. All authors have read and agreed to the published version of the manuscript.

Funding: This work was supported by the Materials & Parts Technology Development Program (20019447) funded By the Ministry of Trade, Industry & Energy (MOTIE, Korea) and Korea Electric Power Corporation (R21XO02-9).

Data Availability Statement: The data presented in this study are available on request from the corresponding author.

Conflicts of Interest: The authors declare that they have no known competing financial interests or personal relationships that could have appeared to influence the work reported in this paper.

References

1. Sun, H.; Xu, X.; Song, Y.; Zhou, W.; Shao, Z. Designing High-Valence Metal Sites for Electrochemical Water Splitting. *Adv. Funct. Mater.* **2021**, *31*, 2009779. [CrossRef]
2. She, Z.W.; Kibsgaard, J.; Dickens, C.F.; Chorkendorff, I.; Norshov, J.K.; Jaramillo, T.F. Combining theory and experiment in electrocatalysis: Insights into materials design. *Science* **2017**, *355*, eaad4998.
3. Wang, N.; Li, L.; Zhao, D.; Kang, X.; Tang, Z.; Chen, S. Graphene Composites with Cobalt Sulfide: Efficient Trifunctional Electrocatalysts for Oxygen Reversible Catalysis and Hydrogen Production in the Same Electrolyte. *Small* **2017**, *13*, 1701025. [CrossRef]
4. Sun, H.; Xu, X.; Kim, H.; Jung, W.C.; Zhou, W.; Shao, Z. Electrochemical Water Splitting: Bridging the Gaps between Fundamental Research and Industrial Applications. *Energy Environ. Mater.* **2022**, e12441. [CrossRef]
5. Chi, J.; Yu, H. Water electrolysis based on renewable energy for hydrogen production. *Chin. J. Catal.* **2018**, *39*, 390. [CrossRef]
6. Kou, T.; Wang, S.; Li, Y. Perspective on High-Rate Alkaline Water Splitting. *ACS Mater. Lett.* **2021**, *3*, 224. [CrossRef]
7. Dionigi, F.; Strasser, P. NiFe-Based (Oxy) hydroxide Catalysts for Oxygen Evolution Reaction in Non-Acidic Electrolytes. *Adv. Energy Mater.* **2016**, *6*, 1600621. [CrossRef]
8. Kim, J.S.; Kim, B.; Kim, H.; Kang, K. Recent Progress on Multimetal Oxide Catalysts for the Oxygen Evolution Reaction. *Adv. Energy Mater.* **2018**, *8*, 1702774. [CrossRef]
9. Yang, R.; Zhou, Y.; Xing, Y.; Li, D.; Jiang, D.; Chen, M.; Shi, W.; Yuan, S. Synergistic coupling of CoFe-LDH arrays with NiFe-LDH nanosheet for highly efficient overall water splitting in alkaline media. *Appl. Catal. B Environ.* **2019**, *253*, 131. [CrossRef]
10. Jiang, D.; Ma, W.; Zhou, Y.; Xing, Y.; Quan, B.; Li, D. Coupling Co_2P and CoP nanoparticles with copper ions incorporated Co_9S_8 nanowire arrays for synergistically boosting hydrogen evolution reaction electrocatalysis. *J. Colloid Interface Sci.* **2019**, *550*, 10. [CrossRef]
11. Yang, Y.; Zhang, K.; Lin, H.; Li, X.; Chan, H.C.; Yang, L.; Gao, Q. MoS_2–Ni_3S_2 Heteronanorods as Efficient and Stable Bifunctional Electrocatalysts for Overall Water Splitting. *ACS Catal.* **2017**, *7*, 2357. [CrossRef]
12. Chen, S.; Kang, Z.; Hu, X.; Zhang, X.; Wang, H.; Xie, J.; Zheng, X.; Yan, W.; Pan, B.; Xie, Y. Delocalized Spin States in 2D Atomic Layers Realizing Enhanced Electrocatalytic Oxygen Evolution. *Adv. Mater.* **2017**, *29*, 1701687. [CrossRef] [PubMed]
13. Xu, X.; Liang, H.; Ming, V.; Qi, Z.; Xie, Y.; Wang, Z. Prussian Blue Analogues Derived Penroseite (Ni, Co)Se_2 Nanocages Anchored on 3D Graphene Aerogel for Efficient Water Splitting. *ACS Catal.* **2017**, *9*, 6394. [CrossRef]

14. Sun, Y.; Zhang, T.; Li, X.; Liu, D.; Liu, G.; Zhang, X.; Lyu, X.; Cai, W.; Li, Y. Mn doped porous cobalt nitride nanowires with high activity for water oxidation under both alkaline and neutral conditions. *Chem. Commun.* **2017**, *53*, 13237. [CrossRef]
15. Peng, X.; Wang, L.; Hu, L.; Li, Y.; Gao, B.; Song, H.; Huang, C.; Zhang, X.; Fu, J.; Huo, K.; et al. In situ segregation of cobalt nanoparticles on VN nanosheets via nitriding of $Co_2V_2O_7$ nanosheets as efficient oxygen evolution reaction electrocatalysts. *Nano Energy* **2017**, *34*, 1. [CrossRef]
16. Wang, Y.; Kong, B.; Zhao, D.; Wang, H.; Selomulya, C. Strategies for developing transition metal phosphides as heterogeneous electrocatalysts for water splitting. *Nano Today* **2017**, *15*, 26. [CrossRef]
17. Li, W.; Zhang, S.; Fan, Q.; Zhang, F.; Xu, S. Hierarchically scaffolded CoP/CoP_2 nanoparticles: Controllable synthesis and their application as a well-matched bifunctional electrocatalyst for overall water splitting. *Nanoscale* **2017**, *9*, 5677. [CrossRef] [PubMed]
18. Jiang, D.; Xu, Y.; Yang, R.; Li, D.; Meng, S.; Chen, M. CoP_3/CoMoP Heterogeneous Nanosheet Arrays as Robust Electrocatalyst for pH-Universal Hydrogen Evolution Reaction. *ACS Sustain. Chem. Eng.* **2019**, *10*, 9309. [CrossRef]
19. Xun, S.; Xu, Y.; He, J.; Jiang, D.; Yang, R.; Li, D.; Chen, M. MOF-derived cobalt oxides nanoparticles anchored on $CoMoO_4$ as a highly active electrocatalyst for oxygen evolution reaction. *J. Alloys Compd.* **2019**, *806*, 1097. [CrossRef]
20. Yu, M.Q.; Jiang, L.X.; Yang, H.G. Ultrathin nanosheets constructed $CoMoO_4$ porous flowers with high activity for electrocatalytic oxygen evolution. *Chem. Commun.* **2015**, *51*, 14361. [CrossRef]
21. Yang, Y.; Wang, S.; Jiang, C.; Lu, Q.; Tang, Z.; Wang, X. Controlled Synthesis of Hollow Co–Mo Mixed Oxide Nanostructures and Their Electrocatalytic and Lithium Storage Properties. *Chem. Mater.* **2016**, *7*, 2417. [CrossRef]
22. Fang, L.; Wang, F.; Zhai, T.; Qiu, Y.; Lan, M.; Huang, K.; Jing, Q. Hierarchical $CoMoO_4$ nanoneedle electrodes for advanced supercapacitors and electrocatalytic oxygen evolution. *Electrochim. Acta.* **2018**, *259*, 552. [CrossRef]
23. Zhang, B.; Liu, G.; Jin, B.; Zhao, L.; Lang, X.; Zhu, Y.; Jiang, Q. $CoMoO_4$/rGO hybrid structure embellished with Cu nanoparticles: An electrocatalyst rich in oxygen vacancies towards enhanced oxygen evolution reaction. *Mater. Lett.* **2021**, *293*, 129741. [CrossRef]
24. Paul, B.; Bhanja, P.; Sharma, S.; Yamauchi, Y.; Alothman, Z.A.; Wang, Z.L.; Bal, R.; Bhaumik, A. Morphologically controlled cobalt oxide nanoparticles for efficient oxygen evolution reaction. *J. Colloid Interface Sci.* **2021**, *582*, 3222. [CrossRef] [PubMed]
25. Lv, X.; Cao, L.; Fu, Y.; Guo, J.; Yang, J.; Huang, Y.; Wang, J. Morphology-controlled synthesis of Cu_2S for efficient oxygen evolution reaction. *J. Electroanal. Chem.* **2022**, *907*, 116020. [CrossRef]
26. Xie, W.; Huang, J.; Huang, L.; Geng, S.; Song, S.; Tsiakaras, P.; Wang, Y. Novel fluorine-doped cobalt molybdate nanosheets with enriched oxygen-vacancies for improved oxygen evolution reaction activity. *Appl. Catal. B Environ.* **2022**, *303*, 120871. [CrossRef]
27. Xu, Y.; Xie, L.; Li, D.; Yang, R.; Jiang, D.; Chen, M. Engineering $Ni(OH)_2$ Nanosheet on $CoMoO_4$ Nanoplate Array as Efficient Electrocatalyst for Oxygen Evolution Reaction. *ACS Sustain. Chem. Eng.* **2018**, *6*, 12. [CrossRef]
28. Guan, X.; Yang, L.; Zhu, G.; Wen, H.; Zhang, J.; Sun, X.; Feng, H.; Tian, W.; Chen, X.; Yao, Y. A hierarchical $CoMoO_4$ nanoparticle decorated nanoplate array as an electrocatalyst toward improved alkaline oxygen evolution reaction. *Sustain. Energy Fuels* **2020**, *4*, 1595. [CrossRef]
29. Luo, J.; Wang, X.; Gu, Y.; Wang, D.; Wang, S.; Li, W.; Zhou, Y.; Zhang, J. Constructing hollow nanocages of Co_3O_4-$CoMoO_4$ heterostructure for efficient electrocatalytic oxygen evolution reaction. *Appl. Surf. Sci.* **2022**, *606*, 154562. [CrossRef]
30. Yang, W.D.; Xiang, J.; Zhao, R.D.; Loy, S.; Li, M.T.; Ma, D.M.; Li, J.; Wu, F.F. Nanoengineering of $ZnCo_2O_4$@$CoMoO_4$ heterogeneous structures for supercapacitor and water splitting applications. *Ceram. Int.* **2023**, *49*, 4422. [CrossRef]
31. Xia, L.; Bo, L.; Shi, W.; Zhang, Y.; Shen, Y.; Ji, X.; Guan, X.; Wang, Y.; Tong, J. Defect and interface engineering of templated synthesis of hollow porous Co_3O_4/$CoMoO_4$ with highly enhanced electrocatalytic activity for oxygen evolution reaction. *Chem. Eng. J.* **2023**, *452*, 139250. [CrossRef]
32. Song, S.; Mu, L.; Jiang, Y.; Sun, J.; Zhang, Y.; Shi, G.; Sun, H. Turning Electrocatalytic Activity Sites for the Oxygen Evolution Reaction on Brownmillerite to Oxyhydroxide. *ACS Appl. Mater. Interfaces* **2022**, *14*, 42. [CrossRef] [PubMed]
33. Du, H.; Pu, W.; Yang, C. Morphology control of Co_3O_4 with nickel incorporation for highly efficient oxygen evolution reaction. *Appl. Surf. Sci.* **2021**, *541*, 148221. [CrossRef]
34. Vinothkumar, V.; Abinaya, M.; Chen, S.M. Ultrasonic assisted preparation of $CoMoO_4$ nanoparticles modified electrochemical sensor for chloramphenicol determination. *J. Solid State Chem.* **2021**, *302*, 122392. [CrossRef]
35. Priya, M.; Premkumar, V.K.; Vasantharani, P.; Sivakumar, G. Structural and electrochemical properties of $ZnCo_2O_4$ nanoparticles synthesized by hydrothermal method. *Vacuum* **2019**, *167*, 307. [CrossRef]
36. Dillip, G.R.; Ramesh, B.; Reddy, C.M.; Mallikarjuna, K.; Ravi, O.; Dhoble, S.J.; Joo, S.W.; Raju, B.D. X-ray analysis and optical studies of Dy^{3+} doped $NaSrB_5O_9$ microstructures for white light generation. *J. Alloys Compd.* **2014**, *615*, 719. [CrossRef]
37. Yan, X.; Tian, L.; Atkins, S.; Liu, Y.; Murowchick, J.; Chen, X. Converting $CoMoO_4$ into CoO/MoOx for Overall Water Splitting by Hydrogenation. *ACS Sustain. Chem. Eng.* **2016**, *4*, 3743. [CrossRef]
38. Hammoodi, O.G.; Tikrity, E.T.B.A.; Hassan, K.H. Sulfur Removal from Iraqi Kerosene by Oxidative Desulfurization Using Cobalt Molybdate-Graphene Composite. *World J. Environ. Sci.* **2014**, *8*, 92.
39. Adabavazeh, H.; Saljooqi, A.; Shamspur, T.; Mostafavi, A. Synthesis of polyaniline decorated with ZnO and $CoMoO_4$ nanoparticles for enhanced photocatalytic degradation of imidacloprid pesticide under visible light. *Polyhedron* **2021**, *198*, 115058. [CrossRef]
40. Qi, J.Q.; Li, S.L.; Sui, Y.W.; He, Y.Z.; Meng, Q.K.; Wei, F.X.; Ren, Y.J.; Jin, Y.X. Solvent dependence on structure and supercapacitor performance of mesoporous $NiCo_2O_4$ grown on nickel foam. *Mater. Res. Exp.* **2017**, *4*, 106302. [CrossRef]
41. Prasad, K.; Reddy, G.R.; Manjula, G.; Park, S.H.; Suh, Y.; Reddy, B.P.; Mallikarjuna, K.; Raju, B.D.P. Morphological transformation of rod-like to pebbles-like $CoMoO_4$ microstructures for energy storage devices. *Chem. Phys.* **2022**, *553*, 111382. [CrossRef]

42. Reddy, G.R.; Reddy, N.R.; Dillip, G.R.; Joo, S.W. In Situ Construction of Binder-Free Stable Battery-Type Copper Cobaltite and Copper Oxide Composite Electrodes for All-Solid State Asymmetric Supercapacitors: Cation Concentration and Morphology-Dependent Electrochemical Performance. *Energy Fuels* **2022**, *36*, 5965. [CrossRef]
43. Wang, F.; Zhao, J.; Tian, W.; Hu, Z.; Lv, X.; Zhang, H.; Yue, H.; Zhang, Y.; Ji, J.; Jiang, W. Morphology-controlled synthesis of $CoMoO_4$ nanoarchitectures anchored on carbon cloth for high-efficiency oxygen oxidation reaction. *RSC Adv.* **2019**, *9*, 1562. [CrossRef] [PubMed]
44. Reddy, G.R.; Dillip, G.R.; Manjunath, G.L.; Joo, S.W. Boosting the Electrochemical Performance of Mn-doped $CuCo_2O_4/CuO$ Heterostructures for All-Solid-State Asymmetric Battery-type Supercapacitors. *J. Electrochem. Soc.* **2022**, *169*, 060549. [CrossRef]
45. Sivakumar, P.; Raj, C.J.; Ramesh, R.; Kulandaive, L.; Park, J.W.; Jung, H. Influence of heat-treatment temperature on the improvement of the electrochemical performance of $CoMoO_4$ nanomaterials for hybrid supercapacitor application. *Ceram. Int.* **2022**, *48*, 29018. [CrossRef]
46. Rajasekhara, R.G.; Sreekanth, T.V.M.; Rajavaram, R.; Borelli, D.P.R.; Dillip, G.R.; Nagajyothi, P.C. Effect of reaction time and PVP contents on morphologies of hierarchical 3D flower-like $ZnCo_2O_4$ microstructures for energy storage devices. *Int. J. Energy Res.* **2020**, *44*, 11233.
47. Sivakumar, P.; Jana, M.; Kota, M.; Jung, M.G.; Gedanken, A.; Park, H.S. Controllable synthesis of nanohorn-like architectured cobalt oxide for hybrid supercapacitor application. *J. Power Sources* **2018**, *402*, 147. [CrossRef]
48. Fang, Y.; Li, X.; Hu, Y.; Li, F.; Lin, X.; Tian, M.; An, X.; Fu, Y.; Jin, J.; Ma, J. Ultrasonication-assisted ultrafast preparation of multiwalled carbon nanotubes/Au/Co_3O_4 tubular hybrids as superior anode materials for oxygen evolution reaction. *J. Power Sources* **2015**, *300*, 285. [CrossRef]
49. Dong, Q.; Wang, Q.; Dai, Z.; Qiu, H.; Dong, X. MOF-Derived Zn-Doped $CoSe_2$ as an Efficient and Stable Free-Standing Catalyst for Oxygen Evolution Reaction. *ACS Appl. Mater. Interfaces* **2016**, *8*, 40. [CrossRef]
50. Akbayrak, M.; Anal, A.M. Metal oxides supported cobalt nanoparticles: Active electrocatalysts for oxygen evolution reaction. *Electrochim. Acta* **2021**, *393*, 139053. [CrossRef]
51. Das, D.; Das, A.; Raghunath, M.; Nanda, K.K. Phosphine-free avenue to Co_2P nanoparticle encapsulated N, P co-doped CNTs: A novel non-enzymatic glucose sensor and an efficient electrocatalyst for oxygen evolution reaction. *Green Chem.* **2017**, *19*, 1327. [CrossRef]
52. Han, L.; Yu, X.Y.; Lou, X.W. Formation of Prussian-Blue-Analog Nanocages via a Direct Etching Method and their Conversion into Ni–Co-Mixed Oxide for Enhanced Oxygen Evolution. *Adv. Mater.* **2016**, *28*, 4601. [CrossRef] [PubMed]
53. Zheng, Z.; Geng, W.; Wang, Y.; Huang, Y.; Qi, T. $NiCo_2O_4$ nanoflakes supported on titanium suboxide as a highly efficient electrocatalyst towards oxygen evolution reaction. *Int. J. Hydrog. Energy* **2017**, *42*, 119. [CrossRef]
54. Liu, M.; Li, J. Cobalt Phosphide Hollow Polyhedron as Efficient Bifunctional Electrocatalysts for the Evolution Reaction of Hydrogen and Oxygen. *ACS Appl. Mater. Interfaces* **2016**, *8*, 3. [CrossRef]
55. Sung, M.C.; Lee, G.H.; Kim, D.W. $CeO_2/Co(OH)_2$ hybrid electrocatalysts for efficient hydrogen and oxygen evolution reaction. *J. Alloys Compd.* **2019**, *800*, 450. [CrossRef]